IEEE Access
Multidisciplinary ⁝ Rapid Review ⁝ Open Access Journal

Received 7 May 2025, accepted 8 June 2025, date of publication 12 June 2025, date of current version 27 June 2025.

Digital Object Identifier 10.1109/ACCESS.2025.3579076

RESEARCH ARTICLE

Joined Spatial and Spectral Segmentation of Hyperspectral Datasets on Historical Art Objects

LINGXI LIU[1,2], AURORE MALMERT[3], EMELINE POUYET[3], SILVIA MIRRI[2], (Member, IEEE), AND GIOVANNI DELNEVO[2], (Member, IEEE)

[1]Department of Art History, Musicology and Theatre Studies, Ghent University, 9000 Ghent, Belgium
[2]Department of Computer Science and Engineering, University of Bologna, 40126 Bologna, Italy
[3]Centre de Recherche sur la Conservation (CRC), Muséum National d'Histoire Naturelle, CNRS, UAR 3224, Ministère de la Culture, 75005 Paris, France

Corresponding author: Giovanni Delnevo (giovanni.delnevo2@unibo.it)

This work was supported by Italia-Slovenia Bilateral Project entitled "Advanced Imaging Technologies for the Study of Works of Art" under Project SI18MO03.

ABSTRACT In the context of clustering and classification, the choice between spatial and spectral features hinges on data characteristics and analytical goals. Spatial features excel in spatially contextualised data like urban planning and object detection, capturing adjacent pixel relationships. Spectral features, prominent in hyperspectral data, shine in tasks requiring precise material identification. However, managing extensive hyperspectral data poses challenges, prompting hybrid approaches for efficient data segmentation. This study presents an innovative data processing pipeline that combines spatial and spectral clustering techniques for the extraction and mapping of spectral signatures in both cinematic films and pointillism painting. We explore Simple Linear Iterative Clustering (SLIC) Superpixel's potential in reducing hyperspectral data while maintaining spectral richness. By optimizing superpixel segmentation and extracting central spectra, we reduce data size significantly. This facilitates applying various machine learning algorithms, especially the soft clustering algorithms Fuzzy C-Means clustering (FCM) and Gaussian Mixture Models (GMM), to classify spectra into distinct colourant groups, identifying complex mixtures and areas of degradation. This research highlights the potential of machine learning in aiding artwork diagnostics, conservation, and restoration, with transferable models for similar scenarios.

INDEX TERMS Machine learning, cultural heritage, hyperspectral imaging, image segmentation, fuzzy clustering, Gaussian mixture models.

I. INTRODUCTION

Art conservation and restoration are complex processes that demand a deep understanding of the materials and conditions of artworks [1]. Traditionally, the identification process requires careful sampling from the artwork, which is usually limited and risky, especially when dealing with precious pieces [2], [3]. In recent years, non-invasive spectral imaging tools have brought new possibilities into the analytical investigation, where the identification and mapping of diverse chemical compounds are enabled by examining characteristic spectral features [4], [5], [6]. Hyperspectral Imaging (HSI) is one of these emerging techniques in the Cultural Heritage (CH) field [7], [8]. It registers a map of the artwork with spectrum collected at each spatial location, forming a 3-dimensional datacube that contains high-resolutional information both spatially and spectrally. However, artworks usually exhibit heterogeneous compositions and complex preservation states, making the identification of material mixtures and the detection of degradation particularly difficult [9]. Furthermore, the precise mapping of such details through the extensive spectral data is a challenging task, demanding more efficient and automatic data segmentation techniques.

In this context, machine learning and statistical algorithms have found fruitful applications in processing the heavy HSI dataset to identify and map distinct material groups. However, methods developed through other fields like remote sensing

The associate editor coordinating the review of this manuscript and approving it for publication was Zhenhua Guo.

or industrial applications is limited in CH application, due to the nature of data and specific goals in analysis. First of all, CH data often involves highly heterogeneous materials like pigments, binders, varnishes, and degradation products that present complex and often intermixed spectral responses and are not always thoroughly studied. The well-established spectral libraries and standardized datasets for classification tasks that are widely used in industrial applications are very limited in CH, making it necessary to rely on expert knowledge and qualitative assessment for interpretation. Furthermore, analysis often targets small and intricate details such as brushstrokes, cracks, and fine visual details that have a higher demand for capturing fine-scale variations, while remote sensing and industrial applications prioritize larger-scale and more homogeneous features.

Due to the critical need to preserve fine details in artworks, existing methods for HSI analysis in the CH field predominantly emphasize the spectral aspect of the data while maintaining the original spatial resolution. Numerous works have applied data dimensionality reduction techniques [10], [11], such as Principal Component Analyses (PCA) [12], t-distributed Stochastic Neighbor Embedding (t-SNE) [13], and Uniform Manifold Approximation and Projection (UMAP) [14], to achieve higher computational efficiency. These methods compress the high-dimensional HSI data into a lower-dimensional space, facilitating fast visualization and subsequent feature extraction and classification. However, these approaches often sacrifice critical spectral details and result in condensed and overlapping data representations, complicating the accurate separation of material mixtures. Another common approach is spectrum-wise classification, where techniques like Spectral Angle Mapper (SAM) [15], [16], [17], Fully Constrained Least Square (FCLS) [18], [19], [20], or Neural Network models [21] are employed to match or unmix spectral signatures. These algorithms enable the accurate identification of pictorial materials but are often constrained by the limited availability of labelled training data and the computational cost of pixel-wise measurements.

In addition to these methods, unsupervised hard clustering algorithms such as K-means [22], [23], Density-Based Spatial Clustering of Applications with Noise (DBSCAN) [24], and Hierarchical Clustering Analysis (HCA) [25] have also been employed to explore material groupings based solely on spectral similarity. While these methods offer a straightforward approach, they become computationally prohibitive when applied to full-resolution hyperspectral images and typically require a preprocessing step, such as PCA or UMAP, to reduce data dimensionality. Moreover, they often struggle to account for the inherent variability and overlap in spectral signatures, and are therefore most commonly used as fast tools for region-of-interest selection rather than for detailed or large-scale segmentation.

While the spectral aspect has seen significant development in analytical techniques, the spatial aspect is often underutilised. Notably, HSI data exhibit redundancies among spatially adjacent pixels due to similarities in material compositions at a small scale. Incorporating the spatial information into classification processes offers great potential to enhance the clustering efficiency. Given the inherent limitations imposed by the nature of the data, we acknowledge that there is a limited number of studies investigating the considered task.

To address this, we propose a novel joint spatial-spectral data segmentation approach to unravel intricate details in art objects. We leverage the Simple Linear Iterative Clustering (SLIC) Superpixel algorithm [26] to spatially segment the data by grouping repetitive spectra into compact and relatively homogeneous regions, providing an optimal balance between data complexity reduction and spectral signature retention. Subsequently, a range of state-of-the-art unsupervised clustering techniques is explored to reveal deeper insights into the underlying patterns within the spectral data, especially the soft clustering algorithms such as Fuzzy C-Means clustering (FCM) [27] and Gaussian Mixture Models (GMM) [28]. The combination of superpixel techniques with clustering algorithms has already demonstrated efficacy in the computer vision field for improved segmentation accuracy with reduced computational time [29], [30]. While such methods have been mainly developed for colour images, they have found promising applications in CH, primarily for fast object extraction and edge detection in document, book, and mural RGB images [31], [32], [33], [34], [35]. For analysing the high-dimensional HSI data, this joint clustering approach is increasingly applied in the remote sensing field to assist urban or terrestrial data classification [36], [37], [38]. Recently, it has also been extended in the domain of CH analysis, particularly in feature delineation within mural paintings in assist for the future restoration works [39], [40]. However, the full capacity of spatial-combined classification to address the challenges of complex material mixtures and degradation has yet to be fully explored.

The efficacy of our proposed approach will be demonstrated through its applications on two distinct historical artworks: one of cinematic films that exhibit non-uniform colour loss and colour balance shifts, and one 19^{th} century Neo-Impressionist painting that presents highly diverse pigment compositions with numerous mixtures on canvas. To benchmark the performance of our method against established techniques, comparative studies are conducted using 1) the SAM Supervised algorithm, and 2) hard clustering algorithms, including HCA, K-means, and DBSCAN, applied both directly to the original spectral datasets and in combination with spatial segmentation via SLIC. The results are evaluated based on segmentation quality, using both qualitative expert validation and quantitative clustering metrics—specifically the Xie-Beni index [41] and Silhouette coefficients [42]. Computational efficiency is also discussed as a key aspect of performance. Our data segmentation pipeline ultimately aims to offer a more nuanced understanding of art materiality, by identifying distinct materials, separating their mixtures, and localising the areas of degradation.

In summary, the main contributions of this study are as follows:

1) We introduce a novel spatial clustering-based data reduction technique to the cultural heritage field, leveraging the SLIC superpixel technique in maintaining spectral richness.
2) Based on the superpixel segmentation, we develop a joint spatial-spectral clustering approach to facilitate efficient material identification and degradation localisation.
3) This research highlights the potential of unsupervised soft clustering techniques in artwork diagnostics, conservation, and restoration, with the flexibility enabled by the possibility matrix and transferable model.

The remainder of this paper is organized as follows. Section II provides comprehensive information on the materials and spectral datasets utilised in this work, the proposed data processing methodology, the comparative studies conducted, and the evaluation strategies. Then, the segmentation results and their evaluation are presented and discussed in Section III and Section IV respectively. Finally, the conclusion and future perspectives of this study are marked in Section V.

II. MATERIALS AND METHODS

A. DATASET DESCRIPTION

1) MATERIALS

Film samples used in this study are provided by ''L'immagine Ritrovata Film Restoration Laboratory'' (Cinematique of Bologna). They come from a historical film fragment manufactured by Fuji Photo Film Co., Ltd. between April and June 1986, with the authorship undetermined. In this paper, four positive film frames, each measuring 34 mm × 19 mm (± 0.5 mm) in physical dimension, are presented (Figure 1a). The transparent support for these films is cellulose acetate, and the yellow, magenta, and cyan dyes are located in distinct layers within the emulsion, forming a trichromatic structure [43]. Due to the unstable nature of these large synthetic organic compounds, the degradation of dyes is inevitable, with different types of dyes exhibiting distinct fading rates over time. Among them, the cyan dyes are the most unstable ones to degrade, followed by the magenta dye and yellow dye. As could be observed in figure 1a, the different stages of degradation are reflected in the gradual transformation of the film's colour, from its original bluish hue (as seen in Film 21) to shades of purple (notably in the left half of Film 23), followed by magenta dominance (most evident in Films 22 and 25), and eventually a yellowish appearance (as indicated by the irregularly shaped stains observed on Films 22 and 25). For historical films like in our case, the degradation is commonly inhomogeneous also from a spatial point of view. These inhomogeneous degradation patterns impose great challenges in the conservation and traditional restoration practice. In this context, digital restoration is advantageous in bypassing the challenging and laborious manual restoration procedure, where the successful identification and segmentation of degradation areas are essential steps.

The 19th century painting ''Au temps d'harmonie (l'âge d'or n'est pas dans le passé, il est dans l'avenir)'' (In the time of harmony: The golden Age is not in the past, it is in the future), oil on canvas, 300 × 400 cm by Paul Signac [44] currently resides in the Town hall of Montreuil (Figure 1b). It was executed between 1893 and 1895 and is nowadays one of the masterpieces of the neo-impressionist artistic movement. The Neo-Impressionists drew inspiration from the colour theory and as such involved juxtaposing small dots of pure colours, sometimes complementary or of varying tones, to obtain the most luminous and vibrant paintings [45], [46]. However, comprehensive material identification of this painting has not been undertaken to date, despite its significance in understanding Paul Signac's creative process, his colour palette, and the practical application of colour theory on his canvas.

2) DATA ACQUISITION

The spectral data of film samples were scanned in the University of Ljubljana by a custom-made hyperspectral camera, which uses the push-broom system with 2,448 across-track pixels and 2,048 wavelengths, composed of an imaging spectrograph (ImSpector V10E, Specim, Finland) and a monochromatic camera (Blackfly S, BFS-U3-51S5M-C, 5 MP, FLIR Integrated Imaging Solutions, Canada) [47]. Spectral images of the film samples were acquired in a reflectance geometry with a broadband LED light source covering the spectral range from 380 nm - 1000 nm. The spectral sampling rate is 0.3 nm in the spectral range of 322.9 - 1025.3 nm, where the considered effective range is from 380 nm to 780 nm. The effective spectral and spatial resolutions of the system were 2.9 nm and 100 μm, respectively, as evaluated by a gas discharge tube and spatial grids used for system calibration. Simple calibration and normalization of the spectra are performed at the time of registration. The initial data contained a lot of noise. To improve the spectral quality, the datacubes were binned by five spectrally and the excessively noisy wavelength range of less than 400 nm and over 750 nm was cropped. Spatially, the uninformative border and perforation areas were also removed, keeping only the image content. Each resulting datacube has a size of 1200 pixels (hor.) x 1000 pixels (ver.) x 180 channels.

Hyperspectral imaging dataset of the 19th century painting, Au temps d'harmonie, was acquired *in situ* with a VNIR (Visible near InfraRed) push-broom PFD4k camera by ©Specim (Oulu, Finland) covering a spectral range from 400 to 1000 nm with 212 bands wavelength channels (spectral resolution of 3.0 nm). In order to scan this large painting, difficult to access, the camera has been equipped with a

FIGURE 1. The optical images of the historical artworks analysed: a) film frames number 21, 22, 23, and 25, b) the original Signac painting and the scanned part (marked in the black rectangle).

long working distance objective, i.e., OLE 140 (focal length 140 mm). The assembled system was mounted on a motorized rotation stage, fixed on a tripod, and set at a distance of 8.7 meters from the painting. The acquisition parameters were set with a scanning speed of 0.02°/s, a frame rate of 5 Hz, an exposure time of 190 ms, and a spectral binning of 4. It resulted in about a 30-minute scan, with a pixel size of 0.50 (v.) x 0.59 (h.) mm. The illumination was provided by two halogen lamps of 2×400 W, located 8 meters away from the painting with a 45° incidence angle. Additionally, twenty LED lamps present within the city hall on both sides of the canvas could not be turned off and participated in the illumination of the painting under study. The data were normalized with dark and white references using the Specim plug-in in ENVI. The white reference corresponded to the white frame surrounding the painting and was saved at the same time as the acquisition. A spectralon was first compared to the frame reflectance signature to ensure the proper diffuse Lambertian properties of the white target. Four acquisitions led to the hyperspectral cube of more than three-quarters of the painting in less than 4 hours. As highlighted in Figure 1b, only the upper part of the painting and several centimetres of the lowest part are missing due to the limited height of the tripod. The first pre-processing of data consisted of the manual stitching of the four datasets using the ENVI software, as well as a spectral crop of the dataset between 440-850 nm and a smoothing of the spectra with Savitzky-Golay filter (13 number of points, 2 polynomial degree) using the Spectronon (©Resonon) software. The final cube is composed of 6481 pixels (hor.) x 4457 pixels (ver.) x 143 channels.

B. METHODOLOGY

The complete data processing pipeline is summarised in Figure 2 and described in detail in the following subsections. First, the acquired HSI data are spatially clustered into homogeneous and compact regions using the superpixel technique. From each superpixel, a representative spatial centroid is extracted, forming a reduced centroid matrix that serves as input for subsequent spectral clustering. Then, the state-of-the-art soft clustering techniques Fuzzy C-means and Gaussian Mixture Models, were applied to this centroid matrix, enabling flexible cluster boundaries and better handling of mixed pixels. As a comparison, the supervised approach (Spectral angle mapper) and hard clustering algorithms, both alone and in combination with SLIC, were also tested. Finally, a label matrix is constructed using the cluster assignments, which is then mapped back to the original image space to visually depict the segmented image.

C. SPATIAL CLUSTERING

SLIC (Simple Linear Iterative Clustering) Superpixel [26] is a widely used algorithm for image segmentation to simplify image processing operations. It divides the image spatially into a number of small and compact regions, within each the superpixel is relatively homogeneous. It has a high potential to reduce the hyperspectral data size, since it can effectively extract the information out of the datacube by grouping similar and repetitive spectra while keeping the full spectral signatures. SLIC works based on the following principles: first, the cluster centres are initialised, i.e., evenly distributed throughout the image, based on the chosen number of superpixels (K). Then, for each cluster centre, the distances between the centre and the pixels in a local neighbourhood are calculated taking into account both the colour similarity and spatial proximity. Each pixel is assigned to the closest cluster centre. Afterwards, the cluster centres are recalculated and updated by taking the mean colour and spatial coordinates of all pixels assigned to them. These

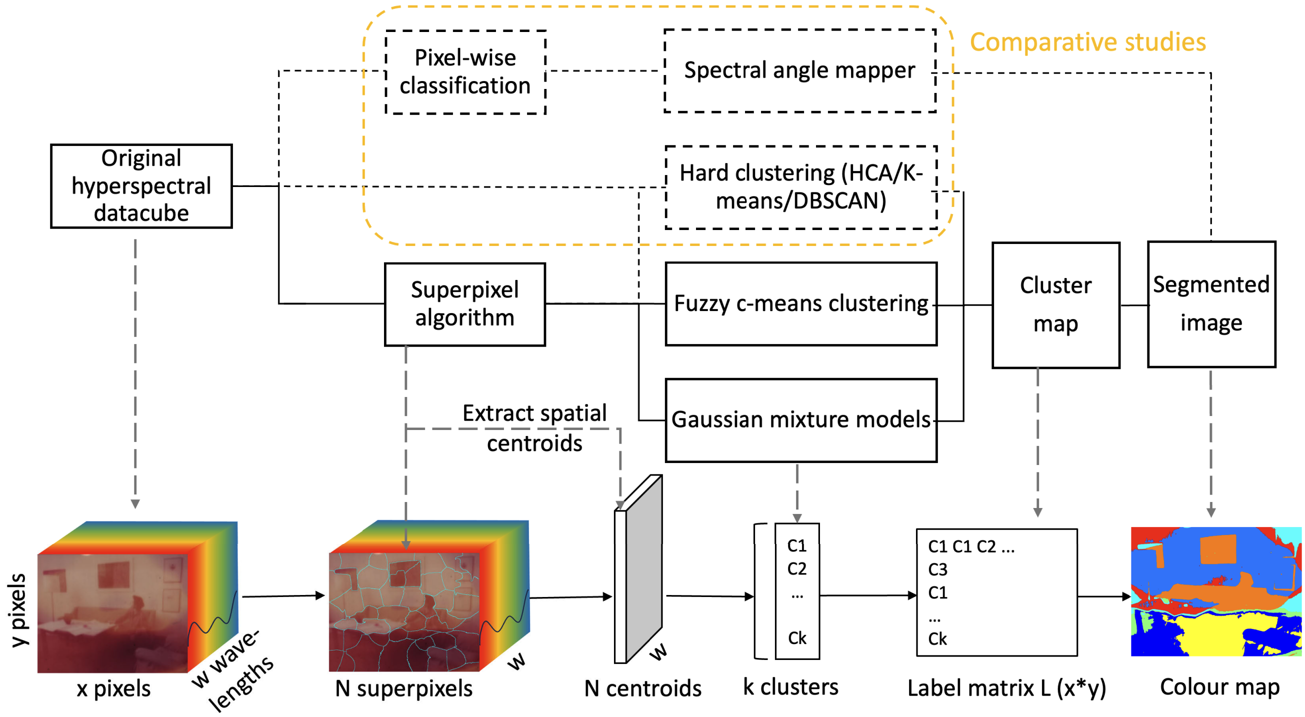

FIGURE 2. **Schematic overview of the data processing methodology employed in this work.**

assignment and update steps are iteratively repeated until reach convergence. During the iterations, the boundaries between superpixels are continually refined also according to the compactness parameter, which specifies the regularity of the superpixel, i.e., the lower the compactness, the better adherence to object boundaries and the more irregularly shaped. A regularisation term is also applied to ensure that each superpixel region is continuous and connected. In the end, a label matrix (L_{slic}) is generated that indicates the membership of each pixel to the superpixels, with the real number of superpixels (N) usually slightly smaller than the input K.

In this step, colour images are used as inputs for simplicity and efficiency during calculation. Multi-channel HSI data are projected and converted respectively into 3-dimensional RGB colour space in the film case and L*a*b* colour space in the Signac painting case using the code provided in [48]. In the latter case, the CIELAB coordinates are preferred, as they enable a subsequent characterisation of the distribution of tone contrasts (L*) and hue variations (a* and b*) in Signac's work. Those resulting images are of the same spatial composition as the HSI cube, and the obtained superpixel label grid L_{slic} could be directly transferred to the HSI data. Then, a spatial centroid approach is adopted to prevent the loss of critical information when averaging the spectra within each superpixel. Specifically, the coordinates of pixels within each superpixel are averaged to get the spatial centre, and the spectra at the spatial centres are extracted to form a new spatial centroid matrix in dimensions of N (number of superpixels) x w (channels). This guaranteed the preservation of unmixed spectral signatures and ensured the precision of material identification. In this way, the HSI data is vastly down-sampled without losing the spectral resolution. The centroid matrix is used as the input in the spectral clustering stage.

D. SPECTRAL CLUSTERING

1) FUZZY C-MEANS CLUSTERING

Fuzzy C-Means clustering (FCM) is a commonly used soft clustering technique that extends the traditional hard clustering to handle uncertainty in cluster assignment [49]. Unlike hard clustering which divides data into distinct clusters, FCM allows data points to belong to multiple clusters in varying degrees, making it especially suitable for pigment mixtures where the division of data is frequently ambiguous. FCM works based on an iterative operation. The optimal number of clusters (K) is determined using the subtractive clustering function in Matlab [50], which estimates the total variations of data in FCM models [51]. With a specified number of desired clusters (K), the FCM algorithm initialises with a random assignment for cluster centres μ. Then, the membership possibility $p_{i,j}$ for each spectrum s_i to each cluster centre μ_j are calculated based on the fuzzy c-means formula:

$$p_{i,j} = \left(\sum_{k=1}^{K} \left(\frac{\|s_i - \mu_j\|}{\|s_i - \mu_k\|} \right)^{\frac{2}{m-1}} \right)^{-1} \tag{1}$$

where m is the fuzziness exponent that defines the overlapping degree of the clusters. Afterwards, the cluster centres μ are updated based on the new membership degrees $p_{i,j}$

$$\mu_i = \frac{\sum_{j=1}^{N} p_{ij}^{m} s_i}{\sum_{j=1}^{N} p_{ij}^{m}}, i \in (1, \ldots, K) \tag{2}$$

where N is the total number of spectra in the dataset. By iteratively updating the cluster centres and recalculating the membership degrees, the objective function J_m is gradually minimised:

$$J_m = \sum_{i=1}^{K} \sum_{j=1}^{N} p_{ij}^{m} D_{ij}^{2} \tag{3}$$

where $D_{i,j}$ is the distance of the j_{th} spectrum to the i_{th} cluster, employing Euclidean metrics. The algorithm finds the optimal partition of the dataset upon convergence when the objective function J_m improves less than a specified minimum threshold. Finally, FCM outputs the list of cluster centres μ and a fuzzy partition matrix p that specifies the cluster membership grades for each data point. The experiment is performed in Matlab using *fcm* function [52].

2) GAUSSIAN MIXTURE MODELS

Gaussian mixture model (GMM) is further explored as a more advanced soft clustering technique that employs probabilistic models to structure complex data distribution [28]. In GMM, each cluster generated is fitted into a Gaussian distribution component defined by its mean μ and covariance matrix Σ, where a vector of mixing coefficients π defines the mixture of different components. For a specified number of components (K), the initial values for component means μ are initialised by applying the K-means algorithm [53], where the covariance matrices are set to be diagonal and identical and the mixing coefficients are set to be uniform for all components. With those initial parameters, the model is iteratively refined using the Expectation-Maximization (EM) algorithm [28], which consists of two main steps: the E-step (Expectation) and the M-step (Maximization). In the E-step, the posterior probability $p_{i,j}$ for the i_{th} spectrum s_i belonging to j_{th} Gaussian component is given by

$$p_{i,j} = \frac{\pi_j \mathcal{N}\left(s_i \mid \mu_j, \Sigma_j\right)}{\sum_{k=1}^{K} \pi_k \mathcal{N}\left(s_i \mid \mu_k, \Sigma_k\right)}, \tag{4}$$

where $\mathcal{N}\left(s_i \mid \mu_j, \Sigma_j\right)$ is the Gaussian probability density function [28]. In the M-step, the algorithm parameters, including the component means μ, covariance matrices Σ, and mixing proportions π, are updated using the posterior probabilities p as weights:

$$\pi_j = \frac{N_j}{N} \quad \text{with} \quad N_j = \sum_{i=1}^{N} p_{i,j}, \tag{5}$$

$$\mu_j = \frac{1}{N_j} \sum_{i=1}^{N} p_{i,j} s_i, \tag{6}$$

$$\Sigma_j = \frac{1}{N_j} \sum_{i=1}^{N} p_{i,j} \left(s_i - \mu_j\right) \left(s_i - \mu_j\right)^{\mathsf{T}}, \tag{7}$$

where N is the total number of data points. These steps are iteratively repeated until the log-likelihood of all data points reach convergence. After the training stage is completed, the optimised component means μ serve as the cluster centres and the posterior probability matrix p contains the membership possibilities to each component of each data point. Furthermore, the output GMM model could be applied to a new data set to predict the cluster belongingness of unseen spectra. The training is performed in Matlab using *fitgmdist* function [54], with regularisation value set to 0.01 and other algorithmic parameters as default.

E. COMPARATIVE STUDIES

To evaluate the performance of our proposed method, we incorporated baseline methods from various perspective for comparison, including 1) the SAM Supervised algorithm, 2) hard clustering algorithms, including HCA, K-means, and DBSCAN, as detailed in the following sections.

1) SUPERVISED CLASSIFICATION

Spectral angle mapper (SAM) is one of the most widely used spectral classification and mapping techniques in CH field [55], [56]. This is a supervised algorithm that relies on the availability of a reference database with known spectra labels. It works based on the principle of comparing the spectral signature of a targeted spectrum in the HSI cube to reference. In this process, each spectrum is transformed into a vector in an n-dimensional scatter plot, where n is the number of wavelengths. The angle α between the reference spectra r (endmembers) and the observed spectra t are then calculated using the *arccosinus* function [57].

$$\alpha = \cos^{-1}\left(\frac{\sum_{i=1}^{n} t_i r_i}{\sqrt{\sum_{i=1}^{n} t_i^2}\sqrt{\sum_{i=1}^{n} r_i^2}}\right) \tag{8}$$

The smaller the angle, the greater the similarity between two spectra (endmembers and observed). An angle threshold is set manually such that the spectrum is classified as similar to an endmember if its angle is smaller than the fixed threshold. The SAM was performed for the painting object solely using the software Spectronon (©Resonon). Ten different endmembers have been selected manually. The Spectral Angle Mapper differs from the previous spectral clustering algorithms in that it operates directly pixel-wise, eliminating the requirement for SLIC superpixel segmentation.

2) HARD CLUSTERING

We compared the performance of our soft clustering method with traditional hard clustering algorithms, namely Hierarchical Clustering Analysis (HCA) [58], K-means [59] and Density-Based Spatial Clustering of Applications with Noise (DBSCAN) [60], applied both directly to the original spectral datasets and in combination with SLIC superpixel.

The Hierarchical Clustering Algorithm (HCA) is an unsupervised hard clustering approach used to divide the data into nested levels of clusters [58]. Alternative to K-means clustering, HCA does not require the specification of a desired number of clusters beforehand. Instead, it forms a hierarchy of clusters that enables the exploration of different levels of details in the data set. However, it relies on pairwise distance calculation to determine the similarity and proximity of the spectra, which has a significant computational cost. In the film case, the Chebychev metric, which is a special form of Minkowski distance (with $p = \infty$) [61], is adopted based on preliminary research detailed in [25]. In the painting case, Cosine metric is selected due to its similarity to the SAM algorithm's settings in distinguishing spectral shapes.

K-means is a popular centroid-based clustering algorithm that partitions the data into a predefined number of clusters [59]. The algorithm minimizes the within-cluster variance, leading to spherical-shaped clusters. One limitation of K-means is that it requires the number of clusters to be specified in advance, which may not be optimal in cases where the number of natural clusters is unknown [62]. Here the same number of clusters were applied for accurate quantitative evaluation.

DBSCAN is a density-based clustering algorithm that identifies clusters by grouping points that are closely packed together, with a minimum number of neighboring points within a defined distance [63]. Unlike K-means, DBSCAN does not require the number of clusters to be specified beforehand, and it can detect clusters of arbitrary shape, making it robust for datasets with noise. However, DBSCAN's performance is highly sensitive to the choice of the two key parameters: the neighborhood radius and the minimum number of points required to form a cluster [64].

These comparative studies are performed in Matlab using the Statistics and Machine Learning Toolbox^{TM} [54].

F. EVALUATION APPROACH

To assess the performance of the proposed clustering algorithm, a comprehensive evaluation was carried out. This involved both qualitative and quantitative analysis. Qualitative evaluation focused on visual inspection of the generated clusters to assess their interpretability and coherence. Quantitative evaluation was performed using two widely recognized clustering evaluation metrics to measure the quality and validity of the clustering results. Computational performance was evaluated both empirically, based on observed runtimes, and analytically through Big O notation to assess theoretical scalability.

With regard to the qualitative one, after obtaining the clustering results, a post-processing step is performed to visualise the image segmentation. The cluster centres are first extracted and plotted to examine the spectral signatures of each group determined. For hard clustering algorithms, the cluster centres are determined by averaging all the spectra assigned to it, while for FCM and GMM, the cluster centres are inherent components of the algorithm and are automatically generated as part of the output. Then, each cluster label is assigned a specific colour to create the colour map. In the case of the film dataset, the jet colour scale is employed to enhance the differentiation among various degradation groups. Conversely, in the analysis of the Signac painting, the actual visual response, represented by RGB values, is calculated for each centre spectrum by transforming the hyperspectral vector to RGB space using the method described in [48]. This approach provides a realistic and intuitive representation of the pigment groups, where the different colours and mixtures are visually identifiable.

To perform image segmentation based on the clustering results, each pixel in the image is assigned a label corresponding to the cluster of the superpixel's centroid. In other words, if the centroid of the j_{th} superpixel is assigned to Cluster C_k, all the pixels within that superpixel are labelled with Cluster C_k. For soft clustering algorithms FCM and GMM, where each spectrum belongs to multiple clusters simultaneously, the cluster with the maximum possibility is assigned. This process propagates the cluster assignments from centroids back to individual pixels, resulting in the creation of a label map. Subsequently, each pixel is coloured with a designated colour, leading to image segmentation where each cluster is visually represented by a unique colour.

The quantitative evaluation was based on two standard clustering evaluation metrics: the Xie-Beni index [41] and the Silhouette coefficient [42]. The Xie-Beni index is an internal clustering evaluation metric that measures the compactness and separation of clusters. A lower Xie-Beni index indicates better clustering performance, as it signifies more compact clusters that are well-separated from each other. Mathematically, the Xie-Beni index is given by:

$$XB = \frac{\sum_{i=1}^{k} \sum_{x \in C_i} ||x - c_i||^2}{n \times min_{i \neq j} ||c_i - c_j||^2} \tag{9}$$

where k is the number of clusters, C_i is the set of points in cluster i, c_i is the centroid of cluster i, and n is the total number of data points. The numerator represents the compactness of the clusters, while the denominator captures the minimum distance between cluster centroids (separation).

The Silhouette coefficient evaluates the consistency within clusters by measuring how similar a data point is to its own cluster compared to other clusters. It ranges from -1 to 1, where higher values indicate better-defined clusters. The Silhouette coefficient S(i) for a data point i is defined as:

$$S(i) = \frac{b(i) - a(i)}{max(a(i), b(i))} \tag{10}$$

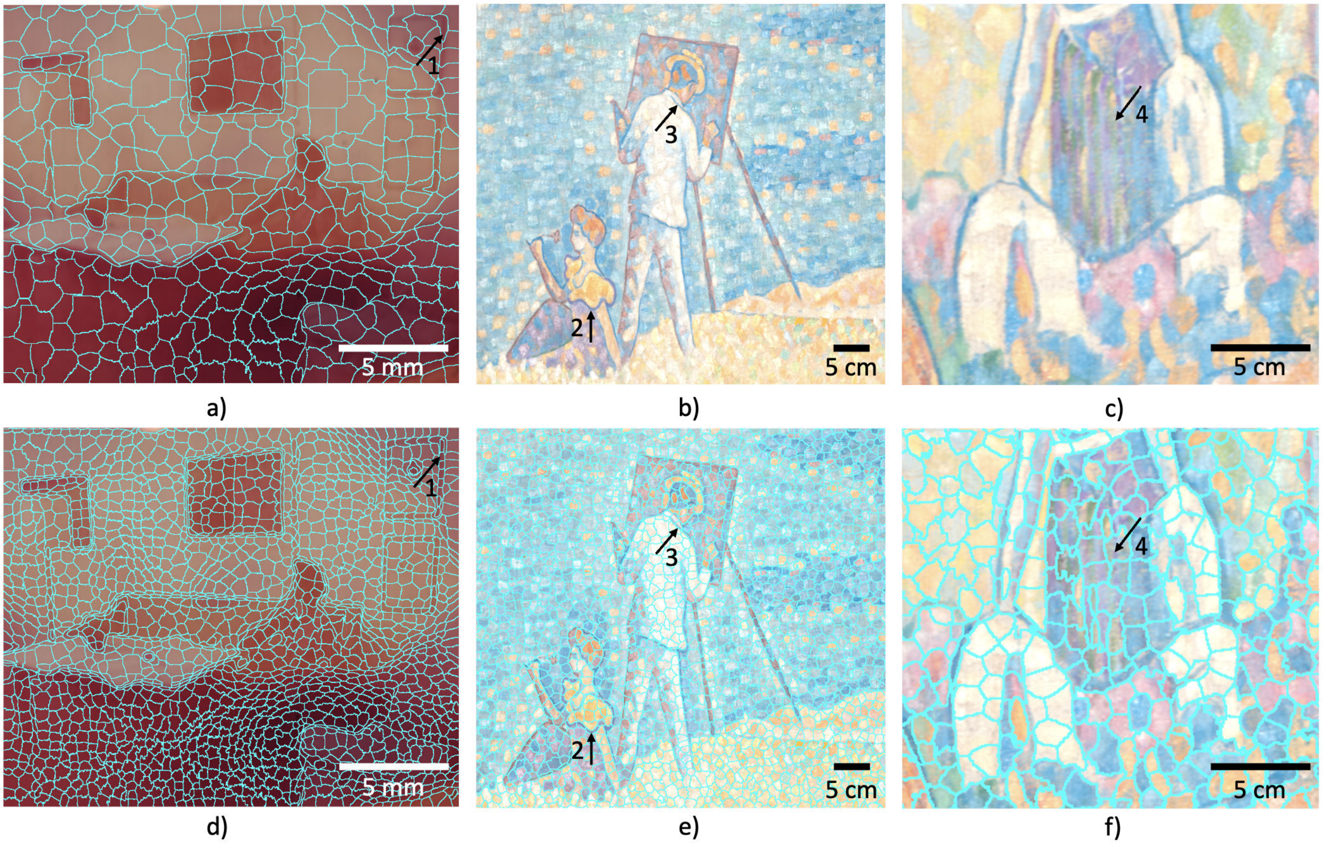

FIGURE 3. Selected details of Superpixel results: a) Film frame 22 with 500 superpixels, b) Film frame 22 with 2,000 superpixels, c) and e) enlarged areas of the original painting, d) and f) enlarged areas of superpixel partition results (k=75,000).

where a(i) is the average distance between point i and all other points in its cluster, and b(i) is the minimum average distance between point i and points nearest neighboring cluster. The overall Silhouette coefficient is the average of S(i) over all data points.

III. RESULTS

A. SPATIAL CLUSTERING RESULTS

SLIC superpixel segmentation was performed on the four film frames and the Signac's painting respectively. The selected results for both cases are illustrated in Figure 3, presenting frame 22 as an example of films and two enlarged areas for Signac's painting. One of the critical input parameters, the desired number of superpixels (k), was investigated for its impact on segmentation. A high number of superpixels can significantly increase the computational load in subsequent processing steps, while an insufficient number can result in inadequate division of sub-areas, such as improper grouping of incoherent pixels and imprecise adhering to object boundaries.

In the case of the film frames, various k values ranging from 500 to 2,000 superpixels were tested. With a compactness of 10, the generated superpixel grids are overall irregularly shaped, conforming to the contours of image content. However, as shown in Figure 3a, when using an insufficient number of superpixels, larger segmented areas are achieved, sacrificing the finer details. For instance, the thin painting frames (indicated by Arrow 1) are not clearly defined and have merged with nearby background pixels on the wall. By increasing the number to 2,000 (Fig. 3d), the finest contours of the human figure, the support of the lamp, and the painting frames are successfully captured and it was determined to be sufficient. Consequently, the four film frames were segmented into 1,822, 1,864, 1,898, and 1,882 superpixels, averaging 659, 644, 632, and 638 pixels per superpixel, respectively. The spatial centroids of each superpixel were extracted and concatenated together to form the input matrix for the following spectra clustering. This reduces the data set size from 4.8 million spectra to 7,466 spectra with variations coming from all degradation areas, maintaining full spectral resolution.

Likewise, in the case of Signac's painting, 75,000 was identified as the most efficient input value for k, while enabling the generation of an output matrix size still within our computational capabilities for subsequent steps. The original image, with spatial dimensions of 6,481 $\times$ 4,457 pixels (nearly 29 million spectra), was effectively partitioned into 74,697 compact and visually coherent regions (superpixels). These superpixels exhibit an average size of 387 pixels, with the smallest and largest superpixels containing 97 and 1,461 pixels respectively. As evident in Figure 3e and f, this number of superpixels facilitated the effective capture of different paint dots, with boundaries conforming to the artistic brush strokes and adjusting to varying sizes. In further detail, the various shades of blue in the sea juxtaposed with each other (as could be seen in the RGB image Fig. 3b) were distinctly separated into discrete superpixels. Similarly, the irregularly shaped pink, blue, and yellow dots placed next to each other in the lower part of Figure 3f were clearly defined. Furthermore, it's noteworthy that the thin outlines are mostly captured as well, exemplified by the female figure in Figure 3e (indicated by Arrow 2). However, the algorithm faces limitations in precisely delineating exceptionally thin outlines, such as that on the male figure (indicated by Arrow 3) in Figure 3b, which is approximately 3 pixels wide. The superimposing straight lines of blue, yellow, and violet colour in the upper part of figure 3c (indicated by Arrow 4) were also beyond the limit of the algorithm to be clearly defined, and compounded by the limited spatial resolution of HSI data.

B. SEGMENTATION ON DEGRADED FILMS

The spectral clustering methodology was applied to the film datasets, with a particular focus on identifying and segmenting areas of dye degradation. In contrast to paintings, where areas painted with distinctive pigments exhibit unique chemical compositions and distinctive spectral characteristics, all film pixels share a common trichromatic structure composed of yellow, magenta, and cyan dyes. These dyes exhibit broad but overlapping absorption features around 430 nm (yellow), 550 nm (magenta), and 650 nm (cyan), with spectral differences primarily related to dye concentration rather than composition. However, degradation introduces a complex challenge. The loss of dye content is both non-uniform across the image and non-linear across the dye types, leading to subtle variations in spectral intensities. This means that pixels subjected to the same level of degradation may exhibit different spectral intensities, complicating segmentation of diverse degradation groups which is crucial for the future digital restoration process.

Since the detailed chemical composition of the degradation products is unknown in this case, a supervised approach was not included in the comparative study. When clustering was applied directly to the full-resolution spectral data, hard clustering algorithms, HCA, K-means, and DBSCAN, failed to produce results within 48 hours due to their high computational demands. In contrast, the superpixel-based pipeline significantly improved efficiency, completing clustering tasks within minutes. Furthermore, despite an extensive grid search to optimize its two primary hyperparameters—neighborhood radius and the minimum number of points to form a cluster—DBSCAN consistently returned only one cluster, suggesting its limited adaptability to this type of high-dimensional spectral data. As a result, only the spatial-spectral joint approach is presented here, focusing on the results obtained using Fuzzy C-Means (FCM) and Gaussian Mixture Models (GMM), with HCA and K-means included as baseline methods for comparison (Figure 4). The effectiveness of the different clustering algorithms is illustrated using a representative single film frame, while the collective segmentation results for all four film frames are provided in the supplementary information.

As introduced in Section II-B, the optimal number of clusters is explored and determined when further increasing the number of clusters does not provide additional information. After a thorough examination, the optimal number of clusters was determined to be 10 (Figure 4a-e). All the tested approached—HCA, K-means, FCM, and GMM—successfully captured the overall data variations. They separated regions with different degradation levels, distinguishing between mildly and extensively degraded areas, and further differentiating within each degradation group between dark and light pixels (1). Figure 4f-j illustrates the spectral centres of these clusters, showing distinctions in spectral intensity.

However, notable confusion was observed with the hard clustering algorithms, which struggled to differentiate regions with subtle spectral differences, especially in light pixel regions where the reflectance intensity differences of less than 0.1. For example, in HCA results, Cluster C9H, partially covering the extensively degraded region, also included a small portion of mildly degraded light pixels, as seen in the upper-left corner of the wall and the newspaper on the desk. Similarly, cluster C5H, characterised by extensively degraded dark pixels, exhibits overlap with the mildly degraded region. This is also observed for the K-means, which grouped both mildly and extensively degraded light pixels together (cluster C1K). This highlights the limitation of hard clustering algorithms to consistently separate subtle spectral differences, where each pixel is forced into a single cluster, potentially overlooking mixed or transitional states. It is also worth noting that while K-means keeps a balanced cluster structure, HCA lacks a mechanism to maximise variations among clusters. Consequently, cluster sizes tend to become imbalanced, with smaller, less meaningful clusters persisting even in the later stages that complicates the interpretation of results.

The results are improved upon transitioning to soft clustering techniques, specifically Fuzzy C-Means (FCM) and Gaussian Mixture Models (GMM). FCM, as shown in Figure 4c, provided better delineation of the extensive degradation states (C1F, C3F, C4F, C5F, and C9F). Especially, the mild degraded cluster C6F is well-defined and effectively separated from the extensively degraded surroundings, including the isolated stain area right above the sofa, which was never identified by the hard clustering algorithms. However, ambiguities remained in clusters C1F, C4F, and C5F, where the light pixels that were less degraded were mixed with dark pixels that have extensively degraded. This ambiguity is also reflected in the spectra centres (Fig. 4h)

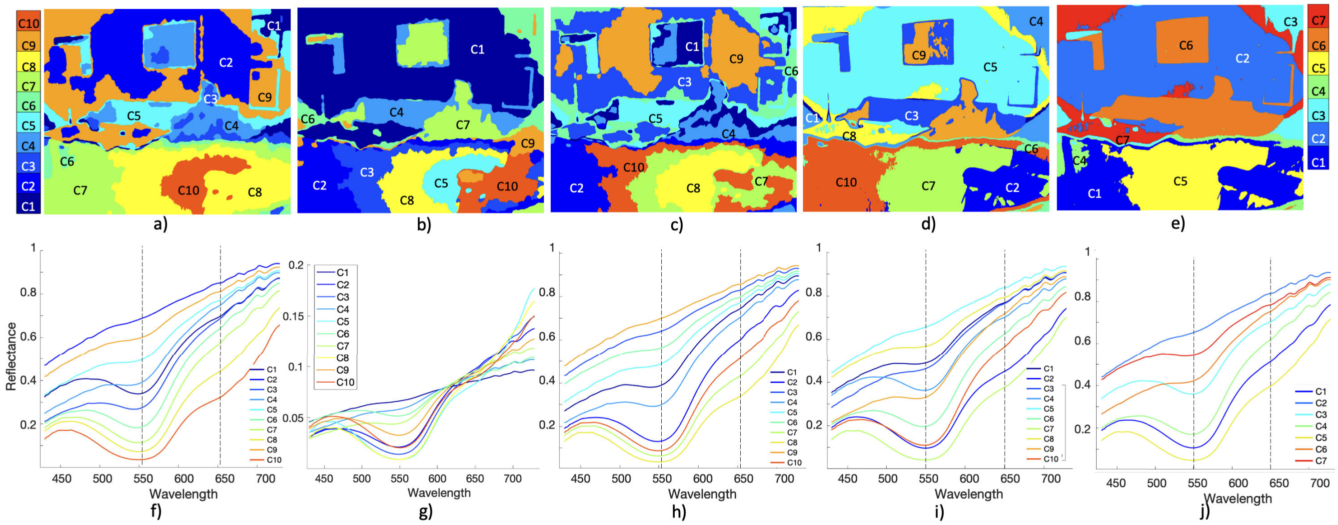

FIGURE 4. Comparison of the spectral clustering results obtained on film frame 22. First row, the segmented images marked with false colour scale via a) HCA (chebychev metric, complete method, 10 clusters), b) K-means (cosine distance, 10 clusters), c) FCM (10 clusters, exponent of 2), d) GMM (10 clusters, regularization = 0.01) and e) GMM (7 clusters, regularization = 0.01) respectively. Second row, the corresponding cluster centres obtained by f) HCA, g) K-means, h) FCM, i) GMM (10 clusters) and j) GMM (7 clusters).

TABLE 1. Summary of the degradation areas segmented via HCA(H), K-means(K), FCM(F) and GMM(G) using 10 clusters, and the segmentation in 7 clusters obtained with GMM(G7). The clusters containing pixels with multiple degradation states are represented in italic.

Degradation Area	**HCA(H)**	**K-means(K)**	**FCM(F)**	**GMM(G)**	**GMM(G7)**
Mild degradation - dark pixel	6, 7, 8, 10	2, 3, 5, 8	2, 7, 8, 10	2, 7, 10	1, 4, 5
Mild degradation - light pixel	1, *5*, *9*	*1*, 6, 9	*1*, *4*, 5, 6	1, 4, 6, 8	3, 7
Extensive degradation - dark pixel	3, 4, *5*	4, 7, 10	*1*, *4*, *5*	3, 9	6
Extensive degradation - light pixel	2, *9*	*1*	3, 9	5,	2

where FCM tends to form cluster centres that differ primarily in intensity but are uniform in spectral characteristics.

GMM outperformed all methods, precisely capturing contours of the extensively degraded regions (C3G, C5G, and C9G), with no misclassifications observed as in HCA, K-means and FCM (Figure 4d). For the first time, the newspaper on the table is clearly partitioned into two degradation stages, C8G (mild degradation) and C3G (extensive degradation). The isolated stain on top of the sofa is accurately classified with C8G as well. Notably, even with only 7 clusters (Figure 4e and j), GMM succeed in capturing the underlying data structure as distinct degradation stages, rather than primarily influenced by overall intensities. This demonstrates its robustness and precision and makes it highly suitable in detecting patterns in overlapping and ambiguous data.

C. SEGMENTATION ON NEO-IMPRESSIONIST PAINTING

The dataset associated with Paul Signac's painting was 6 times larger and more complex than the films studied previously. This dataset exhibited a wider range of variations, including highly diverse spectral signatures and varying intensities, resulting from the different pigment compositions and their numerous mixtures. Nevertheless, the same methodological approach was applied. The series of machine learning algorithms, starting from supervised SAM to the unsupervised clustering techniques HCA (H), K-means (K), FCM (F), and GMM (G), were systematically tested to classify the VIS-NIR spectra into clusters and generate corresponding mappings.

The supervised algorithm Spectral Angle Mapper (SAM) was first employed. As shown Figure 5b, the rough location of the 8 major pure pigments was correctly identified as compared to the original RGB image (Fig. 5a): two cobalt blue ($CoO.Al_2O_3$), one bright and one dark, according to the proportion of white [65], vermilion (HgS) [66], undetermined yellow, viridian green ($Cr_2O_3.2H_2O$) [67], copper and arsenic-based green (Scheele green or emerald green (3 $Cu(AsO_2)_2.Cu(CH_3COO)_2$) [68]) [69], [70], cochineal lacquer [71], [72], undetermined white, cobalt violet ($(Mg_{3-x}Co_x(AsO_4)_2$. x H_2O) [73], [74] and one mixture of vermilion and undetermined yellow. The pure pigments were previously identified using a database of known pigments and selected as endmembers as introduced in section II-E1. Only one pigment mixture (vermilion and yellow) was incorporated as supplementary endmembers due to its predominant presence on the canvas.

However, SAM's results rapidly presented several limitations. First, it is heavily dependent on the choice of representative endmembers, especially when dealing with 29 million spectra. By taking the spectra of the purest

FIGURE 5. Detail of the original image (a) and the segmentation results obtained by b) SAM (10 clusters), c) HCA (20 clusters), d) K-means (25 clusters), e) FCM (25 clusters), and f) GMM (25 clusters).

pigments, all the minor variations in spectra caused by alteration or pigment mixtures were ignored. Second, given the vast number of spectra, determining a suitable threshold became a delicate balance between accuracy and efficiency. A lower threshold value left many pixels unassigned, as marked in black in Figure 5b, while a higher threshold, aimed at efficiently identifying more pixels, increased the likelihood of misclassification, such as assigning the pigment mixtures not included in the endmembers to the wrong group of single pure pigment. Moreover, the insensitivity to variations in spectral intensities of SAM makes it unable to represent the different shades of blue or green used by Signac to create his contrast.

In this context, we found it more promising to reduce the dataset using SLIC and subsequently apply unsupervised clustering algorithms for identifying and mapping a wider range of pigment mixtures and degradations.

As a baseline method, the results obtained by HCA are shown here. The most effective results were obtained with a threshold set at 20 clusters, and the pigments associated with each cluster were identified by comparing the cluster centres to the reference database. As listed in Table 2, this clustering included the same pure pigments, as manually identified with SAM, except for vermilion which is only found mixed with yellow (C6H). Additionally, a larger number of mixtures was distinguished that took into account the variation in overall spectral intensity, resulting from an increasing quantity of white pigments [75]. Consequently, 6 different clusters of cobalt blue (C3H, C4H, C7H, C11H, C12H, C18H), each with varying levels of white pigments, were differentiated and mapped (Fig. 5c). HCA revealed unidentified spectral mixtures characteristic of: i) cochineal lacquer and cobalt blue (C17H - result of superimposition of two dots of cochineal lacquer on cobalt blue), ii) viridian green and yellow (C1H, C10H), and iii) mixture of cobalt blue and viridian green (C8H, C19H). The latter combination was employed very occasionally by Signac to paint the darker, almost black dots on the ''pétanque'' balls, respecting his preferences to avoid all black pigment. In this way, the HCA results offered valuable insights into Signac's palette, particularly with regard to his various mixtures. However, some recurring problems of this algorithm persist. As previously explained on film samples (Section III-B), the size of certain clusters is not homogeneous. Some clusters are too small and could potentially be combined with another cluster without losing information, i.e. C10H of viridian green is composed of only 98 superpixels, while others are overly large, such as C5H of yellow composed of 14 934 superpixels which includes white dots or paler yellows that should be separated into different clusters.

The results of K-means clustering with 25 clusters (Figure 5d), in terms of identification, are comparable to those obtained by HCA, as listed in Table 2. The same pigment mixtures can be identified. However, the distribution of the number of superpixels per cluster is more uniform, ranging from 665 to 4655. The drawback is that the least abundant pigment on the canvas, Scheele or Emerald green, is grouped into a viridian green cluster (cluster C7K) and therefore can not be individually mapped.

FCM and GMM algorithms were then tested. The most effective results were obtained with 25 clusters, as increasing the number of clusters no longer provided additional material identification. Figure 5e and f present the mapping results corresponding to FCM and GMM clusters respectively. As summarised in Table 2, K-means, FCM and GMM algorithms both distinguished the following pure pigments:

TABLE 2. Summary of the pigments identified by cluster number from HCA (H), K-means (K), FCM (F) and GMM (G) approaches. The name of clusters made up of a mixture are represented in italic.

	HCA (H)	K-means (K)	FCM (F)	GMM (G)
Cobalt blue ($CoO.Al_2O_3$)	3, 4, 7, 12, 18, *8*, *11*, *17*, *19*	2, 5, 13, 15, 19, 20, *3*, *4*, *6*, *16*	3, 6, 13, 14, 16, 21, 22, *5*, *9*, *19*	10, 13, 22, *1*, *3*, *8*, *9*, *17*, *24*
Vermilion (HgS)	*6*	*21*	*7*, *18*	*6*, *15*
Viridian green ($Cr_2O_3.2H_2O$)	9, 15, *1*, *8*, *10*, *19*	7, 11, 12, 23, *6*, *9*, *14*, *20*, *22*,	10, *9*, *19*	7, 11, 21, *1*, *12*, *20*, *23*, *24*
Cobalt violet ($(Mg_{3-x}Co_x(AsO_4)_2$. x $H_2O)$)	14	8	2	25
Cochineal lacquer	2, *17*	10, 24, *3*, *4*, *16*	12, 15, *5*	2, 4, *3*, *9*, *17*
Undetermined white	*11*	1	4, 24	19
Undetermined yellow	5, 13, *1*, *6*, *10*	17, 18, 25, *9*, *14*, *21*, *22*	1, 8, 11, 17, 20, 23, 25, *7*, *18*,	5, 16, 18, *6*, *8*, *12*, *15*, *20*, *23*
Scheele/Emerald green (AsCu)	16, 20	-	-	14

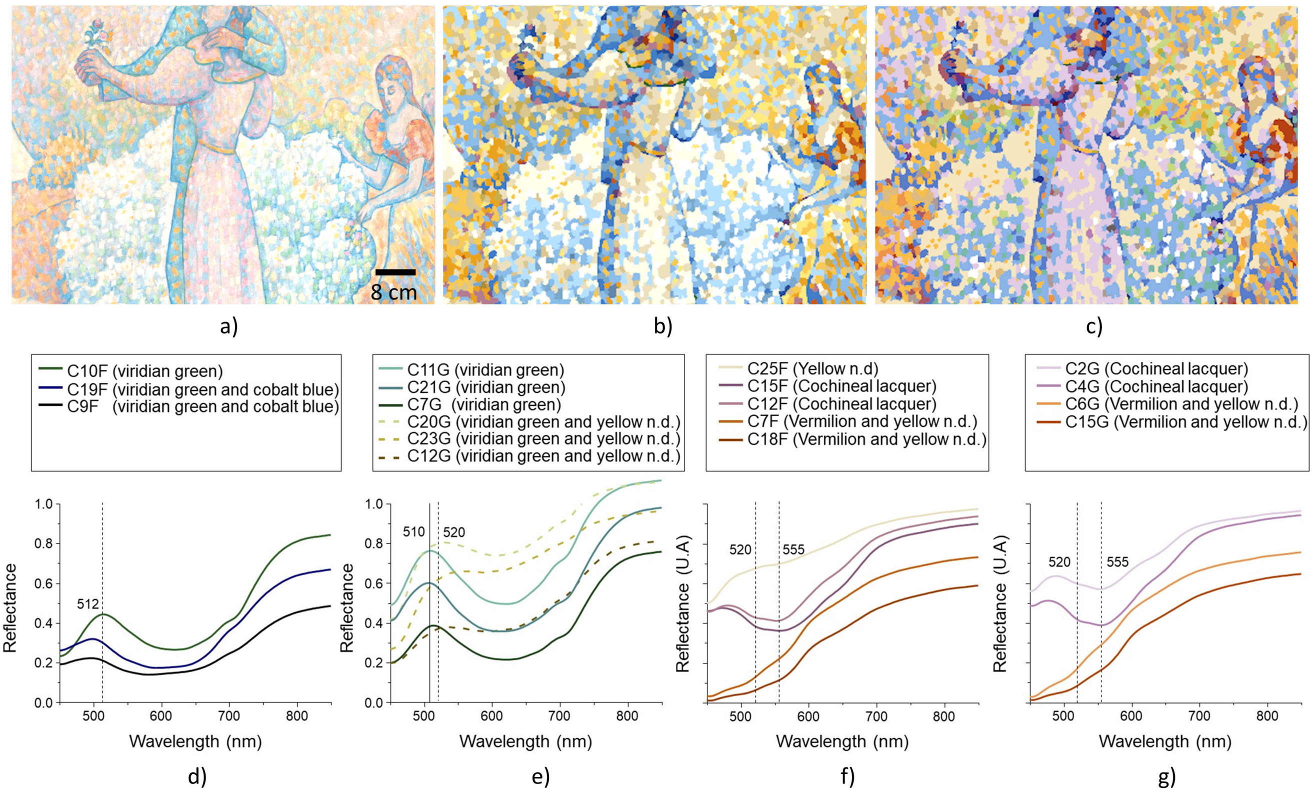

FIGURE 6. Detail area of the original image (a) and the map obtained by b) FCM (25 clusters), and c) GMM (25 clusters), supported by some spectra of green dots identified by d) FCM and e) GMM, and some others characteristic spectra of f) FCM and g) GMM.

cobalt blue, viridian green, cobalt violet, cochineal lacquer, undetermined white, and undetermined yellow like HCA. However, FCM was not successful in distinguishing the Scheele or Emerald green, unlike HCA and GMM algorithms.

In the case of more complex pigment mixtures, soft clustering algorithms have provided insights into a wider range of compositions. Five different mixtures of two pigments have been identified inspecting the FCM spectral centres: once more, i) mixtures of vermilion and undetermined yellow (C7F, 18F) as represented in the figure 6f, ii) mixtures of cochineal lacquer and cobalt blue (C5F), and iii) a mixture of viridian green with cobalt blue (C9F, C19F), shown on the figure 6d. GMM further expended the mixtures distinguished, including vermilion and undetermined yellow (C6G, C15G) as shown in Figure 6g, cobalt blue and undetermined yellow (C8G), as well as mixtures of cochineal lacquer and cobalt blue (C3G, C9G, C17G), and a mixture of viridian green with cobalt blue (C1G, C24G).

Moreover, as shown by figure 6e, three spectra (C12G, C20G, C23G) of the green clusters generated by GMM stand out from the others. Notably, the spectra of these clusters have an absorption maximum shifted to the highest wavelength at 520 nm, while hydrated chromium oxide (viridian green) alone has a maximum absorption at 510 nm (C7G, C11G, C21G in figure 6e, and C10F in figure 6d) [67]. This type of shift is generally due to variations in the pigment particle size or to the presence of another material [8], [76]. The spectra obtained by GMM corresponded in our case to a mixture of viridian green and yellow at 520 nm. These results particularly highlight the contrast of hues, dear to Signac to represent the vibration of his grass. Thus, five different pigment mixtures are distinguished by the FCM, while eleven different mixtures are recognized by the GMM, without taking into account mixtures with white.

The pink dots on the dancer's dress as presented in Figure 6 a-c, illustrated, once again, the difficulties encountered by FCM to distinguish some small variations in the spectrum. GMM demonstrated its ability to effectively distinguish this small pigment subgroup, which is correctly represented as pink in Figure 6c, while in FCM results, these dots were inaccurately represented as yellow (Fig. 6b). Cochineal lacquer is characterised by the two minimum reflections at 520 and 555 nm [71], as precisely reproduced by GMM (C2G and C4G) in Figure 6g. On the contrary, FCM failed to distinguish these unique spectral signatures, misclassifying them along with other yellow dots in the grass (C25F) (Figure 6f).

However, regarding the pure pigment mixed with white, the largest variety of blue tones are identified with FCM, i.e., 7 with FCM (C3F, C6F, C13F, C14F, C16F, C21F, C22F) against 3 with GMM (C10G, C13G, C22G) (Table 2). The different proportions of white mixed in those clusters mainly lead to changes in spectral intensities, without altering the absorption positions [75]. On this point, FCM is more sensitive in capturing the variations in intensities, leading to a better illustration of the contrast of tone used by Signac to represent ripples in the sea (Figure 5d).

D. QUANTITATIVE EVALUATION

This Subsection further evaluates the performance of several clustering algorithms, including HCA, FCM, GMM, K-means, and DBSCAN, on both datasets, the "Painting" and the "Film" ones. A detailed summary of the clustering results is provided in Table 3.

For the "Painting" dataset, significant differences in algorithm performance were observed. HCA, using 20 clusters, exhibited poor results, reflected in a high Xie-Beni Index (XBI) of 7.02 and a low Silhouette Coefficient (SC) of 0.15. These metrics indicate HCA struggled to form compact, well-separated clusters, likely due to the dataset's complex structure. K-means (cosine distance), employing 25 clusters, performed similarly poorly, with an XBI of 5.95 and a negative SC of -0.1, highlighting that cosine distance is unsuitable for this dataset. In contrast, FCM with 25 clusters delivered substantially better performance, achieving an XBI of 0.46, which signifies enhanced compactness and separation. While its SC of 0.38 was not ideal, it was the highest among the algorithms tested, demonstrating FCM's capability to define distinct clusters effectively. GMM, also with 25 clusters, showed moderate results, with an XBI of 2.56 and a negative SC of -0.01, suggesting overlapping clusters and poor cluster definition. However, while GMM did not achieve the highest scores according to standard evaluation metrics, our qualitative assessment revealed that it was the only algorithm capable of accurately capturing subtle patterns associated with certain material groups. This discrepancy can be attributed to the complex nature of our hyperspectral data, where materials frequently exist in blended or transitional states. Such characteristics are penalised by conventional metrics, which inherently favour compact, well-separated clusters and rely on strict distance-based assumptions. As a result, GMM's lower quantitative scores do not necessarily indicate inferior performance, but instead reflect its ability to model the spectral overlap and material heterogeneity that are intrinsic to the dataset.

TABLE 3. Quantitative evaluation of the four clustering algorithms HCA, K-means, FCM, and GMM using Xie-Beni Index (XBI) and Silhouette Coefficients (SC).

Dataset	Algorithm	Clusters	XBI	SC
Painting	HCA	20	7.02	0.15
	K-means	25	5.95	-0.1
	FCM	25	0.46	0.38
	GMM	25	2.56	-0.01
Film	HCA	10	0.38	0.5
	K-means	10	0.47	0.56
	FCM	10	0.37	0.54
	GMM	10	0.87	0.36

The "Film" dataset presented a different performance landscape. HCA, using 10 clusters, achieved an XBI of 0.38 and an SC of 0.5, indicating reasonably compact and well-separated clusters. FCM, also with 10 clusters, slightly outperformed HCA, with an XBI of 0.37 and an SC of 0.54, emerging as the most effective algorithm for this dataset based on these metrics. GMM, with 10 clusters, received a higher XBI of 0.87 and a lower SC of 0.36, suggesting less distinct cluster separation according to standard evaluation metrics. However, qualitative inspection indicated that GMM outperformed the other algorithms in clearly delineating degradation contours, with no misclassification caused by variations in image content or intensity. This suggests that GMM was better able to capture the underlying multi-factor manifolds present in the data, which is not well represented by distance-based measures. Interestingly, K-means (cosine distance), with 10 clusters, achieved notably strong results on the "Film" dataset, obtaining an XBI of 0.47 and the highest SC of 0.56. This is in contrast to its poor performance on the "Painting" dataset. The better performance on "Film" suggests that cosine distance is better suited to datasets where the material groups are fewer and are more linearly separable, aligning with the assumptions of K-means and the clustering metrics, which favour compact and more spherical groups.

In addition, DBSCAN was tested on both datasets. Despite an extensive grid search to optimize its two primary hyperparameters—neighborhood radius and the minimum number of points to form a cluster—DBSCAN consistently returned only one cluster for both datasets. For the ''Painting'' dataset, DBSCAN's failure to identify meaningful clusters was likely due to the complex patterns and overlapping data points inherent to the dataset. Similarly, in the ''Film'' dataset, variations in density and spatial distribution of the data points hindered DBSCAN's ability to form distinct clusters.

IV. DISCUSSION

A. CHALLENGES AND OPPORTUNITIES OF SPECTRAL CLUSTERING

The results presented in Subsection III-B and III-C reveal the challenges and potential solutions for segmenting degradation patterns and analysing spectral data in paintings and films. Hard clustering approaches, such as HCA, provided an initial understanding of cluster distributions but struggled to maximize inter-cluster variance, resulting in imbalanced cluster sizes and difficulties in interpreting finer partitions. The rigid boundaries inherent to hard clustering compounded these issues by causing the spectral centers to be averaged or distorted by boundary pixels, which often include contributions from outliers, making identification more difficult or requiring additional post-processing for smoothing transitions.

Soft clustering methods, specifically FCM and GMM, addressed these challenges more effectively. FCM offered smoother transitions between clusters and better delineation of degradation states compared to HCA. However, it often averaged cluster centres in ambiguous regions, resulting in overlaps. For instance, FCM's cluster C1F in film segmentation encompassed pixels from both highly degraded and less degraded areas, compromising spectral clarity (Table 1). GMM outperformed both HCA and FCM by leveraging Gaussian distribution assumptions to model subtle spectral nuances. This method partitioned ambiguous data patterns effectively, distinguishing fine degradation states. For example, the precise segmentation of the degraded newspaper in frame 22 of the film demonstrated GMM's ability to capture nuanced spectral features and degradation stages with clarity (Figure 4e).

In pigment analysis for Signac's artwork, both FCM and GMM demonstrated distinct strengths. FCM excelled in its sensitivity to intensity variations, effectively partitioning pure pigment groups into nuanced hues. It identified a variety of shades, such as 7 distinct blue tones and 7 yellow tones, providing detailed mappings of tonal variations. In contrast, GMM showed superior precision in capturing subtle spectral changes, accurately differentiating diverse materials and their combinations, even for rare pigments. For instance, GMM identified very small clusters, such as a 96-spectra cluster for pure viridian green and a 137-spectra cluster for Scheele or Emerald green, which FCM merged into larger groups.

These differences between FCM and GMM may be attributed to their initialisation strategies [77]. For Signac's dataset, the size of different pigment groups is unevenly distributed. For instance, there are approximately 24% of cobalt blue dots and 16% of undetermined yellow dots on the canvas, while only 2.5% of cochineal lacquer and 0.1% of Scheele or Emerald green. Consequently, since FCM takes initial cluster centres randomly, larger pigment groups associated with more data points are more likely to be over-represented by assigning more cluster centres relating to it, potentially leading to the neglect and merging of smaller groups into larger clusters. On the contrary, GMM initialises the cluster centres based on a K-means algorithm [53], which initially filtered all data points based on spectral features.

Furthermore, the distance measurement metrics and objective functions employed in the two algorithms could have significantly contributed to the observed differences in results. On one hand, the classical FCM algorithm employed relies on the Euclidean metric as its distance measurement function in the cluster updating stage. This metric naturally tends to yield intensity-based partition and favours the formation of spherical clusters, where data points are distributed more uniformly around a cluster centre. On the other hand, the GMM algorithm models the data points as a combination of multiple Gaussian distribution components with specific mixing coefficients as their weights and optimises the log-likelihood of data points to a component centre. This inherent flexibility allows GMM to form non-spherical and unbalanced clusters that can accurately capture more complex underlying data patterns. As a result, both the FCM and GMM clusters exhibit an average size of 2,988 spectra, while significantly different in the standard deviations (1,009 for FCM and 2,857 for GMM). GMM produced the largest cluster comprising 10,087 spectra (C22G), associated with cobalt blue along with two other substantial clusters each containing over 7,000 spectra (C10G and C13G). In contrast, FCM's largest cluster contains only 4,800 spectra, also in the blue category, accompanied by six moderately-sized clusters (Table 2), each averaging around 3,000 spectra. Conversely, GMM generated very small clusters, including the tiniest one with only 96 spectra dedicated to pure viridian green (C21F), and several other clusters of hundreds of spectra, such as a 137 spectra cluster representing Scheele or Emerald green, a 163 spectra cluster for unmixed white, and a 399 spectra cluster denoting cochineal lacquer. On the other hand, FCM yields just one cluster with fewer than a thousand spectra, C24F, with 686 spectra presenting mixed white. Scheele or Emerald green and cochineal lake are integrated into the larger groups.

These distinctions underscore the complementary nature of FCM and GMM in analyzing spectral data. FCM excels in depicting variations within substantial material categories, making it suitable for visualizing tonal contrasts and transitions, such as those in Signac's seascapes. GMM, on the other hand, is adept at capturing unbalanced or non-uniform data patterns, allowing for precise segmentation of rare pigments and degradation states.

For digital restoration purposes, GMM's ability to generate posterior probability matrices enables smooth transitions along cluster boundaries, reducing the need for additional filtering and ensuring visually coherent results. The advantages of soft clustering techniques, particularly GMM, are evident in their capacity to localize degraded pigments and facilitate high-quality digital restoration and recolorization. These methods provide a more comprehensive understanding of Signac's palette and support future conservation and restoration efforts.

B. PERFORMANCE INSIGHTS AND COMPUTATIONAL TRADE-OFFS IN CLUSTERING ALGORITHMS

The comparison of clustering algorithms highlights significant differences in their ability to handle diverse datasets. FCM consistently delivered a robust balance between low XBI and higher SC, emerging as the most reliable algorithm for clustering tasks across both datasets according to standard evaluation metrics. Its performance indicates a strong capability to handle complex data structures and effectively define distinct clusters. Conversely, K-means (cosine distance) demonstrated dataset-dependent performance. While it performed exceptionally well on the ''Film'' dataset—achieving the highest SC due to the linear separability of clusters in this dataset—it struggled significantly with the ''Painting'' dataset, highlighting its sensitivity to the underlying data structure.

GMM appeared to face challenges in both datasets, as indicated by relatively poor SCI and SC scores, which suggest overlapping clusters and weak separation according to standard metrics. However, these results may not fully reflect the actual performance of GMM, as contradicted by the qualitative inspection. The algorithm's reliance on soft, probabilistic clustering and Gaussian assumptions makes it particularly suited for capturing subtle spectral features and overlapping data structures that are not well represented by distance-based metrics, favoring spherical, well-separated clusters. In contrast, HCA showed moderate success on the ''Film'' dataset but was less effective for the ''Painting'' dataset, reflecting limitations in its ability to handle complex or overlapping cluster structures.

DBSCAN's consistent failure to form multiple clusters underscores its sensitivity to hyperparameter choices and assumptions about cluster density. Its reliance on neighborhood radius and minimum points parameters makes tuning difficult, particularly for datasets with irregular cluster sizes, shapes, or densities. The inability to detect clusters in both datasets suggests that DBSCAN is unsuitable for this type of data or that the natural cluster structure does not conform to its underlying assumptions.

In addition to their clustering performance, the computational complexity of these algorithms varies significantly, influencing their suitability for large-scale applications. HCA has a computational complexity of $O(n^2)$, making it computationally expensive and less practical for large datasets. FCM, with a complexity of $O(n * k * t)$, where n is the number of data points, k is the number of clusters, and t is the number of iterations, offers a more scalable solution while maintaining strong performance. GMM, typically $O(n * k * t)$, incurs additional overhead due to its iterative expectation-maximization process, which can be computationally intensive. K-means (cosine distance) operates with a complexity of $O(n*k*t)$, similar to FCM, but its performance depends heavily on the distance metric and the dataset's characteristics. DBSCAN, with a worst-case complexity of $O(n^2)$ for n data points, is highly sensitive to parameter tuning, further complicating its practical application for large or complex datasets.

Without spatial reduction, the application on the original Film dataset (1200 pixels × 1000 pixels × 180 channels) and Painting dataset (6481 pixels × 4457 pixels × 143 channels) exceeded hardware limitations: HCA and DBSCAN encountered memory exhaustion, while K-means failed to converge after 48 hours. In contrast, the superpixel-based pipeline completed within minutes. When spatial clustering via superpixels was applied, the input size n for all algorithms was significantly lowered, by a factor of 600x for the film dataset and 400x for the painting dataset. This effectively mitigated the computational burden and enabled the use of more sophisticated clustering models on large-scale hyperspectral images.

In conclusion, FCM emerged as the most versatile and robust algorithm, balancing computational efficiency and clustering performance. Its consistent success across datasets underscores its adaptability, making it an excellent choice for applications requiring reliable cluster analysis. GMM offered unique insights in qualitative evaluations, although it was evaluated relatively poorly on standardized metrics due to a mismatch between its probabilistic assumptions and the design of those evaluation criteria. In contrast, the dataset-dependent success of K-means highlights its potential for specific scenarios, provided its limitations are acknowledged. HCA provided helpful initial insights but struggled with more complex data structures. Similarly, DBSCAN was hindered by the inherent assumptions and parameter sensitivities, making them less effective for these datasets.

V. CONCLUSION AND PERSPECTIVES

In this study, we have developed an innovative data processing pipeline combining both spatial and spectral clustering techniques to extract and map spectral signatures, for diverse types of data from both film samples and Paul Signac's painting. These techniques have proven invaluable in uncovering nuanced details that humans cannot determine from the vast amount of data. The SLIC superpixel algorithm has effectively reduced the data size by grouping similar and repetitive spectra from the original dataset while preserving full spectral signatures. Then, the unsupervised clustering techniques have demonstrated their superior ability to reveal underlying patterns of the data, including separating materials of diverse nature, identifying complex mixtures, as well as localising the degradation. Soft clustering algorithms, specifically Fuzzy C-Means (FCM) and Gaussian Mixture Models (GMM), excelled at capturing subtle spectral variations from overlapped data and offered a more nuanced and detailed perspective of the art materials studied. These findings have not only shown the potential of machine learning techniques in aiding artwork diagnostics and conservation, but also provided an invaluable foundation for future restoration works. Furthermore, the models built through the current training samples are transferable to the analysis of artworks with similar compositions. By expanding the included spectral dataset, these models can find wide and efficient applications in numerous similar scenarios.

Future research efforts will also explore advanced parameter settings, such as Mahalanobis distance-based, as introduced by Gustafson and Kessel in 1979 [78], which instead assumes non-spherical cluster shapes and may have improved performance on our dataset, given its flexibility in handling clusters with diverse shapes. It can be set on FCM or GMM with different covariance matrices, to further adapt these techniques to diverse data analysis needs. Moreover the application of multifractal spectrum or Rényi spectrum analysis as a complementary approach to clustering in datasets with non-equally filled clusters could be evaluated. These methods, typically associated with fractal-like structures, hold potential for capturing intricate patterns and distribution characteristics that may elude traditional clustering techniques. By leveraging the ability of multifractal analysis to quantify heterogeneity and complexity across scales, this approach could provide novel insights into the underlying structures of the data, particularly in cases where conventional methods struggle to delineate clusters effectively. Finally, an ablation study could be performed to evaluate the influence of preprocessing activities (e.g., binning, cropping, …) on the model, since they can potentially filter some material signature.

ACKNOWLEDGMENT

The authors are deeply grateful to the Cinematheque of Bologna for providing the film samples for the research. The film's hyperspectral scanning was possible thanks to the financial support provided by Italia-Slovenia Bilateral Project. They would like also to warmly thank the Montreuil city hall and most specifically Aurélie Thuez, Director of the Centre Tignous d'Art Contemporain, for providing and facilitating access to the painting for analysis. They want to thank Emilio Catelli and Jacopo Fadanni for the discussion and insights in future works and thank Laurence de Viguerie and Lucile Brunel-Duverger for their help during the analysis of the neo-impressionist painting. The Observatoire des patrimoines de l'alliance Sorbonne université (OPUS) is thanked for the founding of the Ph.D. thesis of Aurore Malmert.

REFERENCES

[1] G. Artioli, *Scientific Methods and Cultural Heritage: An Introduction To the Application of Materials Science To Archaeometry and Conservation Science*. Oxford, U.K.: OUP Oxford, 2010.

[2] F. G. France, "Advanced spectral imaging for noninvasive microanalysis of cultural heritage materials: Review of application to documents in the US library of congress," *Appl. Spectrosc.*, vol. 65, no. 6, pp. 565–574, Jun. 2011.

[3] B. Brunetti, C. Miliani, F. Rosi, B. Doherty, L. Monico, A. Romani, and A. Sgamellotti, "Non-invasive investigations of paintings by portable instrumentation: The MOLAB experience," *Topics Current Chem.*, vol. 374, no. 1, pp. 41–75, Feb. 2016.

[4] C. Cucci, J. K. Delaney, and M. Picollo, "Reflectance hyperspectral imaging for investigation of works of art: Old master paintings and illuminated manuscripts," *Accounts Chem. Res.*, vol. 49, no. 10, pp. 2070–2079, Oct. 2016.

[5] L. Bertrand, M. Thoury, P. Gueriau, É. Anheim, and S. Cohen, "Deciphering the chemistry of cultural heritage: Targeting material properties by coupling spectral imaging with image analysis," *Accounts Chem. Res.*, vol. 54, no. 13, pp. 2823–2832, Jun. 2021.

[6] M. Alfeld and L. de Viguerie, "Recent developments in spectroscopic imaging techniques for historical paintings–A review," *Spectrochimica Acta B, At. Spectrosc.*, vol. 136, pp. 81–105, Oct. 2017.

[7] M. Picollo, C. Cucci, A. Casini, and L. Stefani, "Hyper-spectral imaging technique in the cultural heritage field: New possible scenarios," *Sensors*, vol. 20, no. 10, p. 2843, May 2020.

[8] H. Liang, "Advances in multispectral and hyperspectral imaging for archaeology and art conservation," *Appl. Phys. A, Solids Surf.*, vol. 106, no. 2, pp. 309–323, Feb. 2012.

[9] Y. Zhao, "Image segmentation and pigment mapping of cultural heritage based on spectral imaging," Ph.D. dissertation, Rochester Inst. Technol., Rochester, NY, USA, 2008.

[10] H. T. Pham, J. Awange, and M. Kuhn, "Evaluation of three feature dimension reduction techniques for machine learning-based crop yield prediction models," *Sensors*, vol. 22, no. 17, p. 6609, Sep. 2022.

[11] E. Abdali, M. J. Valadan Zoej, A. Taheri Dehkordi, and E. Ghaderpour, "A parallel-cascaded ensemble of machine learning models for crop type classification in Google Earth engine using multi-temporal Sentinel-1/2 and landsat-8/9 remote sensing data," *Remote Sens.*, vol. 16, no. 1, p. 127, Dec. 2023.

[12] C. Rodarmel and J. Shan, "Principal component analysis for hyperspectral image classification," *Surveying Land Inf. Sci.*, pp. 115–122, Jan. 2002.

[13] E. Pouyet, N. Rohani, A. K. Katsaggelos, O. Cossairt, and M. Walton, "Innovative data reduction and visualization strategy for hyperspectral imaging datasets using t-SNE approach," *Pure Appl. Chem.*, vol. 90, no. 3, pp. 493–506, Jan. 2018.

[14] M. Vermeulen, K. Smith, K. Eremin, G. Rayner, and M. Walton, "Application of uniform manifold approximation and projection (UMAP) in spectral imaging of artworks," *Spectrochimica Acta A, Mol. Biomolecular Spectrosc.*, vol. 252, May 2021, Art. no. 119547.

[15] J. K. Delaney, J. G. Zeibel, M. Thoury, R. Littleton, M. Palmer, K. M. Morales, E. R. de la Rie, and A. Hoenigswald, "Visible and infrared imaging spectroscopy of Picasso's harlequin musician: Mapping and identification of artist materials in situ," *Appl. Spectrosc.*, vol. 64, no. 6, pp. 584–594, Jun. 2010.

[16] C. Fan, P. Zhang, S. Wang, and B. Hu, "A study on classification of mineral pigments based on spectral angle mapper and decision tree," in *Proc. 10th Int. Conf. Digit. Image Process. (ICDIP)*, Aug. 2018, p. 214.

[17] D. Bai, D. W. Messinger, and D. Howell, "A pigment analysis tool for hyperspectral images of cultural heritage artifacts," *Proc. SPIE*, vol. 10198, pp. 429–443, May 2017.

[18] Z. Gao, M. Du, N. Cao, M. Hou, W. Wang, and S. Lyu, "Application of hyperspectral imaging technology to digitally protect murals in the qutan temple," *Heritage Sci.*, vol. 11, no. 1, pp. 1–16, Jan. 2023.

[19] I. M. Ciortan, T. G. Poulsson, S. George, and J. Y. Hardeberg, "Tensor decomposition for painting analysis. Part 2: spatio-temporal simulation," *Heritage Sci.*, vol. 11, no. 1, p. 84, Apr. 2023.

[20] H. Deborah, M. O. Ulfarsson, and J. Sigurdsson, "Fully constrained least squares linear spectral unmixing of the scream (verso, 1893)," in *Proc. 11th Workshop Hyperspectral Imag. Signal Process., Evol. Remote Sens. (WHISPERS)*, Mar. 2021, pp. 1–5.

[21] L. Liu, T. Miteva, G. Delnevo, S. Mirri, P. Walter, L. de Viguerie, and E. Pouyet, ''Neural networks for hyperspectral imaging of historical paintings: A practical review,'' *Sensors*, vol. 23, no. 5, p. 2419, Feb. 2023.
[22] C. Cucci, A. Barucci, L. Stefani, M. Picollo, R. Jiménez-Garnica, and L. Fuster-Lopez, ''Reflectance hyperspectral data processing on a set of picasso paintings: Which algorithm provides what? A comparative analysis of multivariate, statistical and artificial intelligence methods,'' *Proc. SPIE*, vol. 11784, Jul. 2021, Art. no. 1178404.
[23] N. Chrysogonos, K. Lampropoulos, I. N. Tzortzis, C. Zafeiropoulos, A. Doulamis, and N. Doulamis, ''Evaluating the effectiveness of unsupervised and supervised techniques for identifying deteriorations on cultural heritage monuments using hyper-spectral imagery,'' in *Proc. Int. Conf. Transdisciplinary Multispectral Model. Cooperation Preservation Cultural Heritage*, Jan. 2023, pp. 114–124.
[24] B. Grabowski, W. Masarczyk, P. Głomb, and A. Mendys, ''Automatic pigment identification from hyperspectral data,'' *J. Cultural Heritage*, vol. 31, pp. 1–12, May 2018.
[25] L. Liu, G. Delnevo, and S. Mirri, ''Unsupervised hyperspectral image segmentation of films: A hierarchical clustering-based approach,'' *J. Big Data*, vol. 10, no. 1, p. 31, Mar. 2023.
[26] R. Achanta, A. Shaji, K. Smith, A. Lucchi, P. Fua, and S. Süsstrunk, ''SLIC superpixels compared to state-of-the-art superpixel methods,'' *IEEE Trans. Pattern Anal. Mach. Intell.*, vol. 34, no. 11, pp. 2274–2282, Nov. 2012.
[27] J. C. Bezdek, R. Ehrlich, and W. Full, ''FCM: The fuzzy c-means clustering algorithm,'' *Comput. Geosci.*, vol. 10, nos. 2–3, pp. 191–203, Jan. 1984.
[28] G. J. McLachlan and D. Peel, ''Finite mixture models,'' *Annu. Rev. Statist. its Appl.*, vol. 6, pp. 355–378, Oct. 2019.
[29] T. Lei, X. Jia, Y. Zhang, S. Liu, H. Meng, and A. K. Nandi, ''Superpixel-based fast fuzzy C-means clustering for color image segmentation,'' *IEEE Trans. Fuzzy Syst.*, vol. 27, no. 9, pp. 1753–1766, Sep. 2019.
[30] N. Singh, R. Arya, and R. K. Agrawal, ''Performance enhancement of salient object detection using superpixel based Gaussian mixture model,'' *Multimedia Tools Appl.*, vol. 77, no. 7, pp. 8511–8529, Apr. 2018.
[31] T. Intharah and N. Khiripet, ''MuralCut: Automatic character segmentation from mural images,'' in *Proc. 9th Int. Conf. Electr. Engineering/Electronics, Comput., Telecommun. Inf. Technol.*, May 2012, pp. 1–4.
[32] M. Mehri, N. Sliti, P. Héroux, P. Gomez-Krämer, N. E. B. Amara, and R. Mullot, ''Use of SLIC superpixels for ancient document image enhancement and segmentation,'' *Proc. SPIE*, vol. 9402, Feb. 2015, Art. no. 940205.
[33] Y. Yang and H. Rushmeier, ''Special object extraction from medieval books using superpixels and bag-of-features,'' *J. Electron. Imag.*, vol. 26, no. 1, Nov. 2016, Art. no. 011008.
[34] E. Soyed, R. Chaieb, and K. Kalti, ''Superpixel based segmentation of historical document images using a multiscale texture analysis,'' in *Proc. 8th Int. Conf. Sci. Electron.*, Jul. 2019, pp. 341–351.
[35] C. Hu, X. Huang, G. Xia, Y. Wang, X. Liu, and X. Ma, ''High precision automatic extraction of cultural relic diseases based on improved SLIC and AP clustering,'' *Int. Arch. Photogramm., Remote Sens. Spatial Inf. Sci.*, vol. 43, pp. 801–807, May 2022.
[36] S. M. Borzov and O. I. Potaturkin, ''Spectral–spatial methods for hyperspectral image Classification. Review,'' *Optoelectronics, Instrum. Data Process.*, vol. 54, no. 6, pp. 582–599, Nov. 2018.
[37] L. He, J. Li, C. Liu, and S. Li, ''Recent advances on spectral–spatial hyperspectral image classification: An overview and new guidelines,'' *IEEE Trans. Geosci. Remote Sens.*, vol. 56, no. 3, pp. 1579–1597, Mar. 2018.
[38] M. Imani and H. Ghassemian, ''An overview on spectral and spatial information fusion for hyperspectral image classification: Current trends and challenges,'' *Inf. Fusion*, vol. 59, pp. 59–83, Jul. 2020.
[39] S. Lyu, J. Mao, and M. Hou, ''Mural linear feature enhancement algorithm combining semi-supervised image segmentation and dimensionality reduction,'' *Int. Arch. Photogramm., Remote Sens. Spatial Inf. Sci.*, vol. 46, pp. 423–427, Aug. 2021.
[40] J. Li, D. Xie, M. Li, S. Liu, and C. Wei, ''Pigment identification of ancient wall paintings based on a visible spectral image,'' *J. Spectrosc.*, vol. 2020, pp. 1–8, May 2020.
[41] S. Deng, B. Albert, V. Antoine, and J. Koko, ''A specialized xie-beni measure for clustering with adaptive distance,'' in *Proc. Conf. Eur. Soc. Fuzzy Log. Technol.*, Jan. 2023, pp. 713–724.
[42] A. M. Bagirov, R. M. Aliguliyev, and N. Sultanova, ''Finding compact and well-separated clusters: Clustering using silhouette coefficients,'' *Pattern Recognit.*, vol. 135, Mar. 2023, Art. no. 109144.
[43] H. Wilhelm and C. Brower, *The Permanence and Care of Color Photographs: Traditional and Digital Color Prints, Color Negatives, Slides, and Motion Pictures*. Grinnell, IA, USA: Preservation Pub, 1993.
[44] F. Cachin, *Signac, Catalogue Raisonné De L'oeuvre Peint*. Paris, France: Gallimard, 2000.
[45] O. N. Rood, *Modern Chromatics: With Applications To Art And Industry*, C. K. Paul, Eds., Bristol, U.K.: Read & Co. Books, 1879.
[46] P. Signac, *D'Eugène Delacroix Au Néo-Impressionnisme*. Paris, France: Éditions de la Revue Blanche, 1911.
[47] R. Dolenec, L. Rogelj, J. Stergar, and M. Milanic, ''Modular multi-wavelength LED based light source for hyperspectral imaging,'' in *Proc. Eur. Conf. Biomed. Opt.*, 2019, pp. 56–58.
[48] M. Magnusson, J. Sigurdsson, S. E. Armansson, M. O. Ulfarsson, H. Deborah, and J. R. Sveinsson, ''Creating RGB images from hyperspectral images using a color matching function,'' in *Proc. IEEE Int. Geosci. Remote Sens. Symp.*, Sep. 2020, pp. 2045–2048.
[49] I. Gath and A. B. Geva, ''Unsupervised optimal fuzzy clustering,'' *IEEE Trans. Pattern Anal. Mach. Intell.*, vol. 11, no. 7, pp. 773–780, Jul. 1989.
[50] The MathWorks Inc. (2023). *Subclust Function (r2017a)*. Accessed: Sep. 10, 2023. [Online]. Available: https://it.mathworks.com/help/fuzzy/subclust.html
[51] S. L. Chiu, ''Fuzzy model identification based on cluster estimation,'' *J. Intell. Fuzzy Syst.*, vol. 2, no. 3, pp. 267–278, Aug. 1994.
[52] The MathWorks Inc. (2023). *Fuzzy C-means Clustering*. Accessed: Sep. 10, 2023. [Online]. Available: https://it.mathworks.com/help/fuzzy/fcm.html
[53] D. Arthur and S. Vassilvitskii, ''K-means++ the advantages of careful seeding,'' in *Proc. 18th Annual ACM-SIAM Symposium Discrete Algorithms*, 2007, pp. 1027–1035.
[54] The MathWorks Inc. (2023). *Statistics and Machine Learning Toolbox (r2021b)*. Accessed: Sep. 10, 2023. [Online]. Available: https://www.mathworks.com/help/stats/index.html
[55] C. Cucci, M. Picollo, L. Chiarantini, G. Uda, L. Fiori, B. De Nigris, and M. Osanna, ''Remote-sensing hyperspectral imaging for applications in archaeological areas: Non-invasive investigations on wall paintings and on mural inscriptions in the pompeii site,'' *Microchemical J.*, vol. 158, Nov. 2020, Art. no. 105082.
[56] F. Daniel, A. Mounier, J. Pérez-Arantegui, C. Pardos, N. Prieto-Taboada, S. F.-O.-D. Vallejuelo, and K. Castro, ''Hyperspectral imaging applied to the analysis of Goya paintings in the museum of Zaragoza (Spain),'' *Microchemical J.*, vol. 126, pp. 113–120, May 2016.
[57] F. A. Kruse, A. Lefkoff, J. Boardman, K. Heidebrecht, A. Shapiro, P. Barloon, and A. Goetz, ''The spectral image processing system (SIPS)—Interactive visualization and analysis of imaging spectrometer data,'' *Remote Sens. Environ.*, vol. 44, nos. 2–3, pp. 145–163, Jan. 1993.
[58] F. Murtagh and P. Contreras, ''Algorithms for hierarchical clustering: An overview,'' *WIREs Data Mining Knowl. Discovery*, vol. 2, no. 1, pp. 86–97, Jan. 2012.
[59] K. P. Sinaga and M.-S. Yang, ''Unsupervised K-means clustering algorithm,'' *IEEE Access*, vol. 8, pp. 80716–80727, 2020.
[60] W. Lai, M. Zhou, F. Hu, K. Bian, and Q. Song, ''A new DBSCAN parameters determination method based on improved MVO,'' *IEEE Access*, vol. 7, pp. 104085–104095, 2019.
[61] P. Grabusts, ''The choice of metrics for clustering algorithms,'' in *Proc. Environment. Technologies. Resources Proc. Int. Sci. Practical Conf.*, vol. 2, 2011, pp. 70–76.
[62] A. Fahim, ''Finding the number of clusters in data and better initial centers for K-means algorithm,'' *Int. J. Intell. Syst. Appl.*, vol. 12, no. 6, pp. 1–20, Dec. 2020.
[63] D. Deng, ''DBSCAN clustering algorithm based on density,'' in *Proc. 7th Int. Forum Electr. Eng. Autom. (IFEEA)*, Sep. 2020, pp. 949–953.
[64] K. Khan, S. U. Rehman, K. Aziz, S. Fong, and S. Sarasvady, ''DBSCAN: Past, present and future,'' in *Proc. 5th Int. Conf. Appl. Digit. Inf. Web Technol. (ICADIWT)*, Feb. 2014, pp. 232–238.
[65] M. Bacci and M. Picollo, ''Non-destructive spectroscopic detection of cobalt(II) in paintings and glass,'' *Stud. Conservation*, vol. 41, no. 3, pp. 136–144, Jan. 1996.
[66] M. Aceto, A. Agostino, G. Fenoglio, A. Idone, M. Gulmini, M. Picollo, P. Ricciardi, and J. K. Delaney, ''Characterisation of colourants on illuminated manuscripts by portable fibre optic UV-visible-NIR reflectance spectrophotometry,'' *Anal. Methods*, vol. 6, no. 5, pp. 1488–1500, 2014.

[67] R. Newman, *Artists' Pigments A Handbook of Their History and Characteristics*, vol. 3. Washington, DC, USA: National Gallery of Art, 1997.
[68] I. Fiedler and M. A. Bayard, *Artists' Pigments A Handbook of Their History and Characteristics*. Washington, DC, USA: National Gallery of Art, vol. 3, 1997.
[69] C. Herm, "Emerald green versus Scheele's green: Evidence and occurrence," in *Proc. 7th Interdiscipl. ALMA Conf.*, Bratislava, Slovakia, Feb. 2020, pp. 189–202.
[70] N. F. Barnes, "Color characteristics of Artists' pigments," *J. Opt. Soc. Amer.*, vol. 29, no. 5, p. 208, 1939.
[71] B. Fonseca, C. Schmidt Patterson, M. Ganio, D. MacLennan, and K. Trentelman, "Seeing red: Towards an improved protocol for the identification of madder- and cochineal-based pigments by fiber optics reflectance spectroscopy (FORS)," *Heritage Sci.*, vol. 7, no. 1, p. 92, Nov. 2019.
[72] A. Casini, C. Cucci, M. Picollo, L. Stefani, and T. Vitorino, "Creation of a hyper-spectral imaging reference database of red lake pigments," *COSCH e-Bulletin*, vol. 2015, pp. 1–6, Jan. 2015.
[73] M.-C. Corbeil, J.-P. Charland, and E. A. Moffatt, "The characterization of cobalt violet pigments," *Stud. Conservation*, vol. 47, no. 4, pp. 237–249, Dec. 2002.
[74] F. Casadio, A. Bezúr, I. Fiedler, K. Muir, T. Trad, and S. Maccagnola, "Pablo picasso to jasper johns: A Raman study of cobalt-based synthetic inorganic pigments," *J. Raman Spectrosc.*, vol. 43, no. 11, pp. 1761–1771, Nov. 2012.
[75] R. Johnston-Feller, *Color Science in the Examination of Museum Objects: Nondestructive Procedures*. Los Angeles, CA, USA: The Getty Conservation Institute, 2001.
[76] A. M. Gueli, G. Bonfiglio, S. Pasquale, and S. O. Troja, "Effect of particle size on pigments colour," *Color Res. Appl.*, vol. 42, no. 2, pp. 236–243, Apr. 2017.
[77] Y. Zhang, G. Wang, F. Chung, and S. Wang, "A fuzzy system with common linear-term consequents equivalent to FLNN and GMM," *Int. J. Mach. Learn. Cybern.*, vol. 13, no. 5, pp. 1475–1492, May 2022.
[78] D. Gustafson and W. Kessel, "Fuzzy clustering with a fuzzy covariance matrix," in *Proc. IEEE Conf. Decis. Control including 17th Symp. Adapt. Processes*, Jan. 1978, pp. 761–766.

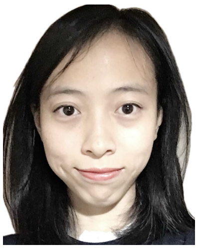

LINGXI LIU received the M.S. degree in science for the Conservation and Restoration of Cultural Heritage and the Ph.D. degree in cultural and environmental heritage from the University of Bologna, in 2020 and 2024 respectively. She is currently a Postdoctoral Research in the ERC Consolidator Grant project ARTDETECT: A New Connoisseurship, Ghent University, with the primary focus on modern style paintings. Her research interests include the application of analytical imaging techniques and machine learning algorithms for the technical analysis of artworks.

AURORE MALMERT received the M.S. degree in analytical sciences from the University of Strasbourg, France, in 2022. She is currently pursuing the Ph.D. degree, funded by Sorbonne University, within the Centre de Recherche sur la Conservation (CRC), Paris, France. Her thesis research focused on the color and materiality of late 19th-century neo-impressionist paintings, using non-invasive analysis techniques.

EMELINE POUYET received the M.S. degree in archaeometry and the Ph.D. degree in ID21 beamline from European Synchrotron Radiation Facility, Grenoble, France, in 2010 and 2014, respectively. She is currently a CNRS Researcher with the Centre de Recherche sur la Conservation (CRC). Her research activities are focused on using infrared and X-ray-based techniques to achieve molecular, elemental, and structural characterization of complex and heterogeneous samples from cultural heritage artifacts.

SILVIA MIRRI (Member, IEEE) received the M.S. degree and the Ph.D. degree in computer science from the University of Bologna, Italy, in 2002 and 2007, respectively.

From 2008 to 2020, she was a Research Assistant at the Department of Computer Science and Engineering, University of Bologna, where she is currently an Associate Professor. She authored more than 170 papers, including 38 articles in scientific journals. Her research interests include human–computer interaction, ranging from content adaptation, and transcoding for multimedia digital content to the accessibility of digital technologies to meet users with disabilities needs. She has investigated HCI topics related to specific contexts, such as digital humanities and cultural heritage, smart environments, and industry 4.0.

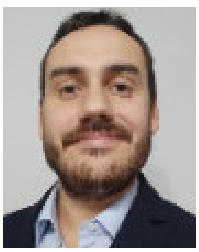

GIOVANNI DELNEVO (Member, IEEE) received the B.S. degree in computer science and information technology, the M.S. degree in computer science and engineering, and the Ph.D. degree in data science and computation from the University of Bologna, Bologna, Italy, in 2013, 2016, and 2022, respectively.

Since 2023, he has been a Junior Assistant Professor at the Department of Computer Science and Engineering, University of Bologna, Italy. His research interests include human–AI interaction, machine learning, and human–computer interaction.